Preseismic Velocity Changes Observed from Active Source Monitoring at the Parkfield SAFOD Drill Site

Fenglin Niu[1], Paul G. Silver[2], Thomas M. Daley[3], Xin Cheng[1], Ernest L. Majer[3]

[1]*Department of Earth Science, MS-126, Rice University, 6100 Main St., Houston, TX 77005*

[2]*Department of Terrestrial Magnetism, Carnegie Institution of Washington, 5241 Broad Branch Road, N.W., Washington, DC 20015, USA*

[3]*Earth Sciences Division, Lawrence Berkeley National Laboratory, 1 Cyclotron Road, Berkeley CA 94720, USA*

Measuring stress changes within seismically active fault zones has been a long-sought goal of seismology. Here we show that such stress changes are measurable by exploiting the stress dependence of seismic wave speed from an active source cross-well experiment conducted at the SAFOD drill site. Over a two-month period we observed an excellent anti-correlation between changes in the time required for an S wave to travel through the rock along a fixed pathway – a few microseconds--and variations in barometric pressure. We also observed two large excursions in the traveltime data that are coincident with two earthquakes that are among those predicted to produce the largest coseismic stress changes at SAFOD. Interestingly, the two excursions started approximately 10 and 2 hours before the events, respectively, suggesting that they may be related to pre-rupture stress induced changes in crack properties, as observed in early laboratory studies[1-2].

It is well known from laboratory experiments that seismic velocities vary with the level of applied stress[3-5]. Such dependence is attributed to the opening/closing of microcracks due to changes in the stress normal to the crack surface[6-8]. In principle, this dependence constitutes a stress meter, provided the induced velocity changes can be

measured precisely and continuously. Indeed, there were several attempts in the 1970s to accomplish this goal using either explosive or non explosive surface sources[9-11]. The source repeatability and the precision in traveltime measurement appeared to be the main challenges in making conclusive observations.

With the availability of highly repeatable sources, modern data acquisition systems, and advanced computational capability, Yamamura *et al.*[12] showed compelling evidence that seismic velocity along a baseline in a vault near the coast of Miura Bay, Japan, responds regularly to tidal stress changes. Silver *et al.*[13] found an unambiguous dependence of seismic velocity on barometric pressure from a series of cross-well experiments at two test sites in California. The stress sensitivity depends primarily on crack density and has a strong nonlinear dependence on confining pressure. Consequently, crack density is expected to decrease rapidly with depth as should stress sensitivity. It is thus unclear whether the stress-induced velocity variations observed at shallow depths[12-13] are still detectable at seismogenic depth.

To explore stress sensitivity at seismogenic depth, we have conducted an experiment at Parkfield where adjacent deep wells, the SAFOD (San Andreas Fault Observatory at Depth) pilot and main holes (Figure 1), are available. Accurately located seismicity together with the availability of high-quality geophysical data in the Parkfield region make it one of the best areas to detect temporal changes related to the earthquake cycle. A specially-designed 18-element piezoelectric source and a three-component accelerometer were deployed inside the pilot and main holes, respectively, at ~1 km depth (see methods). The experiment was conducted for ~2 months: 10/29/05-11/29/05 and 12/11/05 -1/10/06. We fired a pulse with a width of 1 ms 4 times per second and recorded 200 ms long data with a sampling rate of 48,000 Hz. The waveforms were automatically stacked in groups of 100 shots, resulting in 1 record (Figure 2) acquired every 27 seconds (2 additional seconds were needed in storing the data).

To enhance the signal-to-noise ratio (SNR) of the data, we further stacked the raw seismograms in sets of 100. This stacking procedure reduced the data to one stack every 45 minutes. The 45-minute stacked records were then processed with a bandpass filter of 1- 5 KHz before the traveltime analysis. We used a cross-correlation-based method to estimate the delay time, which permits sub-sample precision (see methods). No smoothing and/or filtering were applied to the measured delay time series. The error in delay time measurement was estimated to be $\sim 1.1\times10^{-7}$ s based on SNR analysis (see methods), and this estimate was confirmed by comparing measurements from consecutive recordings. Since the nominal traveltime of the S-wave coda along the baseline is about 10 ms, the detectable threshold of velocity perturbation is $\sim 1.1\times10^{-5}$, or 11 ppm.

We measured the delay times of the S wave and the S wave plus its coda up to 20 ms with respect to a fixed reference trace for each period (Figure 3). The measurements show daily cycles that are well correlated with the temperature record (Figure 3). Silver *et al.*[13] found that this temperature sensitivity originates from the electronics of the recording system rather than from changes in the subsurface velocity field. We excluded the measurements of the first few days to allow the source and sensor to be stabilized at their locations. We also removed the linear trend from the data as was done by Silver et al[13]. In general, the delay times of the coda are about twice as large as those of the S wave, suggesting that they are caused by a change in the velocity of the bulk media, as the coda travels longer in the media and thus is expected to accumulate a larger traveltime anomaly. The delay time closely follows the barometric pressure changes for the first period (Figure 3a).

After removing the temperature effect from the measured delay time variations (Figure 3a), we obtained a delay time change of ~3.0 μs in the first period. The corresponding velocity perturbation is about 3×10^{-4}, about an order of magnitude higher

than the detectable threshold. During the same time period, change in barometric pressure is ~1.3 KPa. We used a linear regression to estimate the velocity stress sensitivity and obtained a value of 2.4×10^{-7} Pa^{-1}. We also calculated the predicted solid Earth tides at the site in the same period and found that the tidal stress varies within 240 Pa, nearly an order of magnitude smaller than changes in barometric pressure. Thus the traveltime changes induced by tidal stress are on the order of 10^{-7} s, close to the measurement error and thus are predicted to be undetectable.

The negative correlation between traveltime and barometric stress can be further seen in the delay time data through the 9^{th} day of the second period after which time the relationship starts to break down. We observe instead two prominent excursions in the delay time data that are not seen in the barometric pressure record. It is also confirmed that the two excursions were not caused by precipitation or instrumentation. The amplitudes of the two excursions are ~5.5 μs and ~1.5 μs, respectively, over the nominal ~10 ms coda traveltime. Using our measured stress sensitivity of 2.4×10^{-7} Pa^{-1}, the corresponding stress changes are 2.3 KPa and 625 Pa for the first and second peak, respectively.

In order to evaluate the possibility for a tectonic cause for the excursions, we examined the seismicity around the SAFOD site occurring in the experiment period (Figure 4a). The first peak appears to correspond to the largest earthquake occurring in this period (date: *12/24/05 10:10:57.21, location: 35.9970 -120.5565 3.88 km, magnitude: M3.00,* hereafter M3 event), while the second peak corresponds to the second closest (1.5 km) event to the experiment site (date: *12/29/05 01:32:50.87, location: 35.9788 -120.5397 1.82 km, magnitude: M0.98,* hereafter M1 event). The closest event is about 1.3 km away from our site, but its size is only *M0.34* and thus should not have a large effect at the site.

We calculated the predicted static stress change at SAFOD associated with these two earthquakes. The near-field static displacement at a location **r** with respect to the earthquake is proportional to $M_o r^{-2}$, where M_o is the seismic moment[14]. The spatial derivative of displacement, strain, thus should be ~ $M_o r^{-3}$. The static stress change at **r** is $\Delta\sigma = a\frac{\mu L^2 D}{r^3} = a\frac{\mu(D/L)}{(r/L)^3} = a\frac{\Delta\sigma_o}{\hat{r}^3}$, where $\Delta\sigma_o$ is the average static stress change along the fault, $\hat{r}$ is the characteristic distance measured in fault lengths (L), D is slip on the fault, and a is a scaling constant equal to $1/(6\pi)$[14]. If we assume a static stress change in the range of 3 to 10 MPa[15-16], then the static coseismic stress change at the SAFOD site is estimated to be ~250 – 833 Pa for the M3 event, which is a few times lower than the total stress change (2.3 KPa) calculated from the amount of delay time during the first excursion. The predicted static stress changes at the SAFOD site calculated from the entire local seismicity catalog are shown in Figure 4b. Here we used all the events that occurred within 10 km of the site and made a time series of the coseismic stress changes. The M3 earthquake obviously has the largest effect at the experiment site. The second largest peak around day 20 corresponds to a relatively deep event (date: *11/22/05 03:38:02.13, location: 36.0100 -120.5692 depth: 5.07 km, magnitude: M2.6*), which is not observed in the delay time data. The third peak corresponds to the M1 event. It is not clear to us why the larger M2.6 is not observed while the smaller M1 event shows clearly in the delay time data. But we noticed that data collected in the second month had a better SNR than those of the first month. The associated stress change of the M2.6 thus might be below the resolution of the first-month data.

Coseismic change was also observed in other geodetic data. We found a step-function change from the borehole fiber-optic strainmeter data at SAFOD (Figure 4a inset) as well as from the surface creepmeter data at Middle Mountain (Figure 4b). The static strain change observed at SAFOD is ~20-25 nanostrain, corresponding to a coseismic stress change of ~600-750 Pa, which is of the same order of magnitude as our estimate. On the other hand, there were no obvious changes in the SAFOD GPS, or the

FLT and DLT strainmeter records (Figures 4b). The lack of an observable coseismic signal at these sites is, however, predicted by the theoretical amplitude.

The coseismic offset recorded by the SAFOD strainmeter is not obviously present in the delay time data measured either from the manually-stacked 45-minute-per-sample data or from the delay times calculated from the 27-second-per-sample raw data. The derivative of the delay time series (dotted line in Figure 4c), however, does reveal that the largest offset of the entire two-month observing period occurred ~30 s after the M3 earthquake. This suggests that there was a small coseismic change in the delay time data. The lack of a stronger coseismic signal in the delay time data may imply that the velocity changes we observed here are mainly the result of a poroelastic[17] rather than an elastic response to abrupt stress changes.

The two traveltime excursions appear to possess significant preseismic components. The first excursion was observed to start at 23:34 pm of 12/23/05, while the M3 earthquake occurred at ~10.6 hours later, 10:10 am of 12/24/05 (Figures 4c). The excursion reached a maximum right after the earthquake, peaking at 21:21 pm of 12/24/05. The excursion thus has a clear preseismic component besides the coseismic/postseismic changes. The preseismic and coseismic/postseismic components account for ~46% and ~54% of the total change. This is also true for the second excursion. Its onset is around 22:59 pm of 12/28/05, about 2.5 hours before the occurrence of the M1 earthquake (1:32 am of 12/29, Figure 4c).

With the available geodetic instrumentation, it was impossible to further evaluate the preseismic component. The most direct test would have been with the SAFOD borehole strainmeter data. Unfortunately, the low frequency component is severely contaminated by surface temperature variations and is unusable for periods longer than a few minutes, and is thus not useful in confirming the two low-frequency excursions

(Zumberge, pers. comm.). All other instrumentation is either too far away or not sufficiently sensitive to observe even the coseismic offset. Historically, there has been an absence of preseismic signals in geodetic observations, such as a borehole strainmeter. We suggest that this may be the result of two differences between such instruments and our "stress meter". First, our basic measurement is not strain, but rather a stress-induced change in the effective elastic constants of a poroelastic medium, mediated by variations in crack properties and fluid flow. These changes may register only weakly on a strainmeter, a GPS, or a creepmeter. Second, a conventional strainmeter measures local change in the volume immediately surrounding the instrument while our measurements reflect stress/strain changes occurring over a volume sampled by the coda waves that could be orders of magnitude larger.

We hypothesize a change in effective elastic moduli prior to rupture such as a sudden increase in micro crack density, a phenomenon related to dilatancy and observed in many laboratory studies[1-2]. As such, further continuous seismic monitoring might provide an effective tool for understanding the stress changes that accompany and perhaps precede seismic activity.

Method summary

We used a specially built piezoelectric source and a "Geode" recorder to generate and record seismic waves travelling along a ~10 m baseline near the San Andreas Fault at ~1 km depth. A cosine fitting method was employed to estimate the S-wave traveltime to sub-sample precision.

Methods

Data acquisition system. Our acquisition was conducted with a combination of commercial and specially-built equipment. The specially-built components are the

piezoelectric source and the high voltage amplifier used to power it. The source includes 18 cylindrical rings of piezoelectric ceramic (lead zirconate titanate) epoxied together and wired for positive and negative voltage on the inner and outer surfaces. The source was fluid coupled to the well casing. A three-component accelerometer was clamped to the well casing to provide coupling and reduce relative motions between the source and receiver. We used a commercial recording system, a "Geode" manufactured by Geometrics, which has a 24 bit analog-to-digital converter. An air conditioner and heater were used to maintain the recording system electronics within a temperature range of about ±1°C.

Triggering was used in our data recording system. The digitizer continually samples the data, and receives a trigger that will generally be between two digitized samples. Including a section of pre-trigger data, the time series is interpolated and re-sampled, so that the new time series begins at the time of the trigger. This start time is not exact, and, at a sampling rate of 48,000/s, this time is computed to the nearest 20^{th} of a sample (Geometrics engineering, personal communication). Thus there is a delay time measurement error that will be at most a 40^{th} of a sample (half-way between samples), and the average error will be an 80^{th} of a sample, assuming that the errors are uniformly distributed. This corresponds to an average error of 260 ns per trigger. The error in the stacked data decreases by a factor of $N^{1/2}$, assuming the errors are uncorrelated. For $N=100$, we obtain a timing error of 26 ns.

Optimum Experimental Design. As shown in *Silver et al.*[13], there is an optimum distance between the source and receiver that minimizes the detectable threshold of subtle velocity changes:

$$N = Q / \pi \qquad (1)$$

Here N is the number of wavelengths between the source and receiver and Q is the quality factor. At the SAFOD site, Q is around 200, which gives N =64. If we assume the S wave velocity to be 2.8 m per ms, then the wavelength of the signal with a dominant frequency of 2 KHz is about 1.4 m, so the optimum distance is ~90 m. Since it was necessary to perform the experiment in the available boreholes, our cross-hole distance was limited to 10 m, which while not optimal still provided us with a good signal to noise ratio.

Sub-sample delay time estimate (DTE). In this study, we employed a cosine fitting method to estimate sub-sample delay time in time domain[18-19]. Given the largest sample of the correlation function, *cc(0)*, and its two neighbours *cc(-1)* and *cc(1)*, the estimated sub-sample shift is given by following expression:

$$\tau = \alpha \,/\, \arctan\left(\frac{cc(-1)-cc(1)}{2cc(0)\sin\alpha}\right), \tag{2}$$

where,

$$\alpha = \arccos\left(\frac{cc(-1)+cc(1)}{2cc(0)}\right). \tag{3}$$

Error estimation. *Silver et al.*[13] derived a low bound of the error in delay time measurements:

$$\sigma_{DTE} \geq \frac{1}{2\pi f_0 \cdot SNR}. \tag{4}$$

Here f_0 is the dominant frequency of the source pulse, and *SNR* is the signal to noise ratio. Equation (4) indicates that the *SNR* is the only parameter that controls the precision in our delay time estimation when the digitizing error is much less than the background noise in this regime. The precision is not controlled by the sampling rate of the digitizer so it is possible to obtain sub-sample-interval measurements of the delay time. The dominant frequency of our data is 2 KHz and the *SNR* is around 700 for the

45-minute stacked data, resulting in a best achievable precision of ~1.1×10^{-7} s, or 110 ns in the delay time estimate.

We also measured delay time between each two consecutive samples, which follows a Gaussian distribution with a standard deviation of ~80 ns and ~50 ns for the first and second recording period, respectively. In general they are comparable to or even better than the theoretical low bound in equation (4). Since there is contribution from the actual stress-induced velocity perturbations in the measurement, our actual precision can be better than the measured standard deviations. Thus the lower bound appears to be larger than the true DTE error. One possible explanation is that the *SNR* is significantly underestimated, as the noise is estimated from a time window before the first arrival, which actually contains a considerable amount of non-random electronic noise known as crosstalk, and non-random "wrap-around" noise from the previous shot.

The precision discussed here does not include other systematic non-random noise, such as changes in the source pulses, errors in trigger timing and digitizer's clock. Such systematic errors could lead to a long-term trend in TDE. To estimate these effects, we also recorded the source pulse waveform in addition to the data. We employed the same method to measure the variation in the source pulse width. Changes in the source pulse width are between ±20 ns. This indicates that our source pulse generator and recording system were very stable in the two periods and timing error in the digitizer clock was also very small.

1. Brace W. F., Paulding, B. W. & Scholz, C. H., Dilatancy in the fracture of crystalline rocks. *J . Geophys. Res.* **71**, 3939-3953 (1966).
2. Scholz, C. H., Microfracturing and the inelastic deformation of rock I: compression. *J . Geophys. Res.* **73**, 1417-1432 (1968).

3. Birch, F., The velocity of compressional waves in rocks to 10 kilobars, part 1. *J. Geophys. Res.* **65**, 1083–1102 (1960);

4. Birch, F., The velocity of compressional waves in rocks to 10 kilobars, part 2. *J. Geophys. Res.* **66**, 2199–2224 (1961)

5. Nur, A., & Simmons, G., The effect of saturation on velocity in low porosity rocks. *Earth Planet. Sci. Lett.* **7,** 183-193 (1969).

6. Walsh, J. B., The effect of cracks on the compressibility of rock. *J. Geophys. Res.* **70,** 381-389 (1965).

7. Nur, A., Effects of stress on velocity anisotropy in rocks with cracks. *J. Geophys. Res.* **76**, 2022-2034 (1971).

8. O'Connell, R. J. & Budiansky, B., Seismic velocities in dry and saturated cracked solids, *J. Geophys. Res.* **79**, 5412-5426 (1974).

9. De Fazio, T. L., Aki, K. & Alba, J., Solid earth tide and observed change in the in situ seismic velocity. *J. Geophys. Res.* **78**, 1319-1322 (1973).

10. Reasenberg, P. & Aki, K., A precise, continuous measurement of seismic velocity for monitoring in situ stress. *J. Geophys. Res.* **79**, 399-406 (1974)

11. Leary, P. C., Malin, P. E., Phinny, R. A., Brocher, T. & Voncolln, R., Systematic monitoring of millisecond traveltime variations near Palmdale, California. *J. Geophys. Res.* **84**, 659-666 (1979).

12. Yamamura, K. et al., Long-term observation of in situ seismic velocity and attenuation. *J. Geophys. Res.* **108**, 10.1029/2002JB002005 (2003).

13. Silver, P. G., Daley, T. M., Niu, F. & Majer, E. L., Active Source Monitoring of Cross-Well Seismic Traveltime for Stress-Induced Changes. *Bull. Seismol. Soc. Amer.* **97**, 281-293 (2007).

14. Aki, K. & Richards, P. G., *Quantitative Seismology* (W. H. Freeman, New York, 1980).

15. Abercrombie, R. E., Earthquake source scaling relationships from -1 to 5 M_L using seismograms recorded at 2.5-km depth. *J. Geophys. Res.* **100**, 24,015-24,036 (1995).

16. Rubin, A. M. & Gillard, D., Aftershock asymmetry/rupture directivity among central San Andreas fault microearthquakes. *J. Geophys. Res.* **105**, 19,095-19,109 (2000).

17. Segall, P., Jonsson, S. & Agustsson, K., When is the strain in the meter the same as the strain in the rock?, *Geophys. Res. Lett.* **30**, doi:10.1029/2003GL017995 (2003).

18. Cespedes, I., Huang, Y., Ophir, J. & Spratt, S., Methods for estimation of sub-sample time delays of digitized echo signals, *Ultrason. Imaging* **17**, 142-171 (1995).

19. De Jong, P. G. M., Arts, T., Hoeks, A. P. G. & Reneman, R.S., Determination of tissue motion velocity by correlation interpolation of pulsed ultrasonic echo signals, *Ultrason. Imaging,* **12**, 84-98 (1990).

20. Unsworth, M., Bedrosian, P., Eisel, M., Egbert, G., & Siripunvaraporn, W., Along strike variations in the electrical structure of the San Andreas Fault at Parkfield, California. *Geophys. Res. Lett.* **27**, 3021-2024 (2000).

We would like to thank the NSF funded SAFOD program and all the people involved for providing the experiment site, Rob Trautz of LBNL for supplying the barometric pressure logger, Dr. Mark Zumberge of University of California San Diego for providing the SAFOD strainmeter data, Don Lippert and Ramsey Haught of LBNL for helping the field work, and two anonymous reviewers for constructive comments. This work is supported by NSF, Rice University, Carnegie Institution of Washington and Lawrence Berkeley National Laboratory of the U.S. Department of Energy under Contract No. DE-AC02-05CH11231.

Correspondence and requests for materials should be addressed to F.N. (e-mail: niu@rice.edu).

Figure 1. Map of the experiment site. (a) Earthquakes that occurred during the experiment period are shown by circles. The M3 and M1 events are shown as red and green circles, respectively. Star indicates the Parkfield SAFOD drill site, where the experiment was conducted. Triangle and squares show the locations of the Middle Mountain creepmeter, the Donalee and Frolich Gladwin borehole tensor strainmeters. (b) A vertical section (schematic) of the SAFOD main and pilot holes. Red vertical lines indicate the source and receiver locations. Background image is electrical resistivity[20] with blue (red) corresponding to relatively high (low) resistivity.

Figure 2. An example of the raw seismograms obtained from a horizontal component in the two periods. Inset shows the first 30 ms of the waveforms. Both are filtered with a band pass filter of 1 to 5 KHz.

Figure 3. Delay times estimated from time windows which contain the S-wave arrival and the S-wave arrival plus the coda are shown with the barometric pressure, temperature and precipitation for the first (a) and second period (b). Elapsed time is calculated from 11/02/05 00:00:00, UT.

Figure 4. (a) Depth distribution of earthquakes that occurred in the experimental period. Red square, red and green circles indicate the SAFOD experiment site, the M3 and M1 earthquake, respectively. Inset shows the SAFOD strainmeter record which shows a step-function coseismic strain change. The low frequency content of the strainmeter data is severely contaminated by surface temperature variations, and is consequently not suitable for analysis. (b) Creep measurement at Middle Mountain, GPS measurement of fault-parallel motion at the SAFOD site, and the calculated static coseismic stress changes at the SAFOD experiment site for all of the earthquakes are shown along with the delay times estimated from the S wave plus its coda for comparison. Dashed

lines indicate the time when the M3 and M1 earthquakes occurred. Note that the amplitude of the stress change of the M3 event (~0.5 KPa) is saturated in this plot. (c) Predicted coseismic stress changes at SAFOD for earthquakes occurring between December 22 of 2005 (day 50) and January 1 of 2006 (day 60) indicated by shading in (b) are shown with the delay time estimation. Stress changes between day 55 and 60 are amplified by a factor of 10. Dotted line is the derivative of the delay time series. Notice that the largest change occurred about ~30 s after the M3 earthquake.

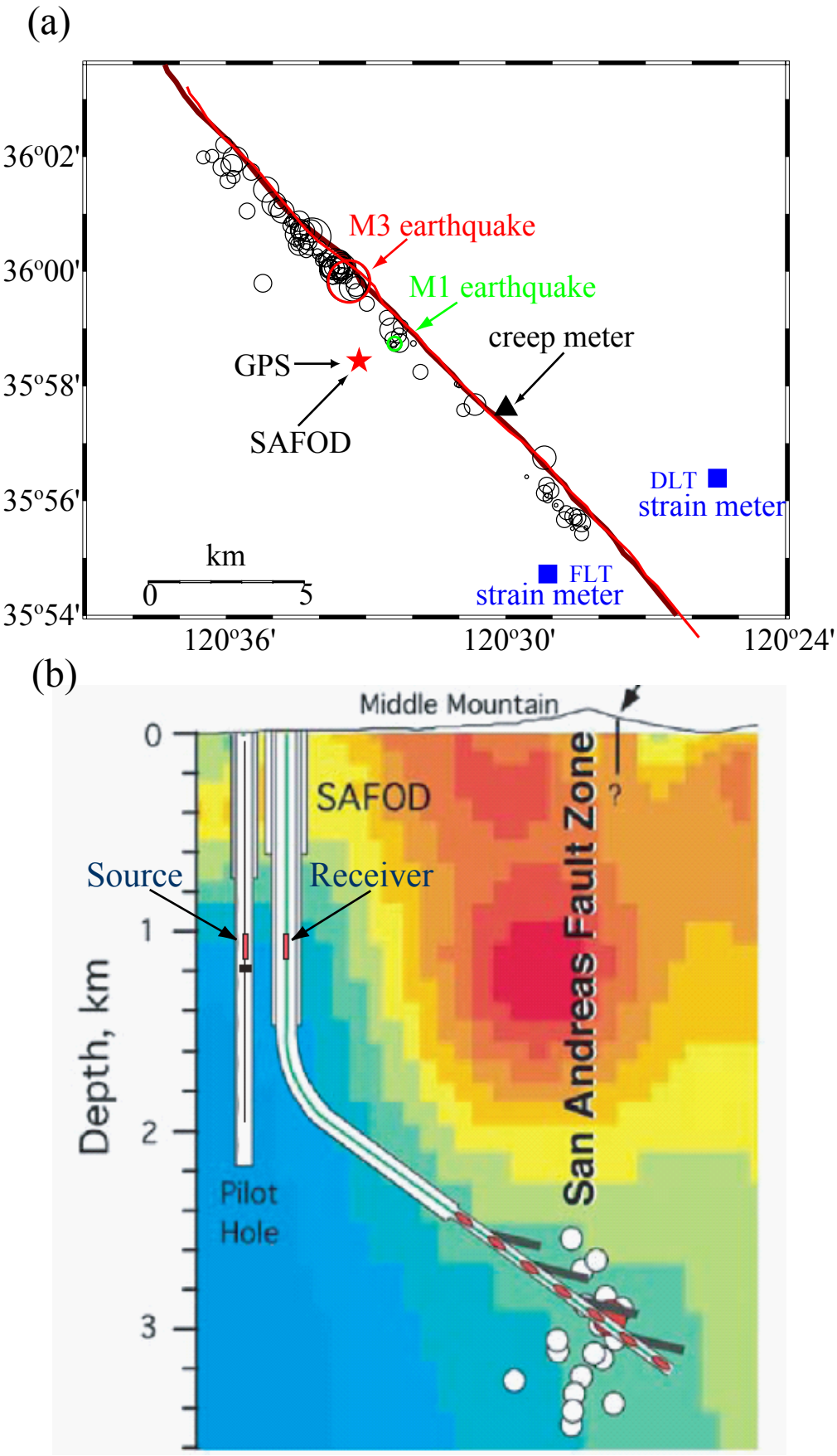
(a)
36°02'
36°00'
35°58'
35°56'
35°54'
120°36'
120°30'
120°24'
M3 earthquake
M1 earthquake
creep meter
GPS
SAFOD
DLT
strain meter
FLT
strain meter
km
0
5
(b)
Middle Mountain
SAFOD
Source
Receiver
Depth, km
0
1
2
3
Pilot
Hole
San Andreas Fault Zone
?

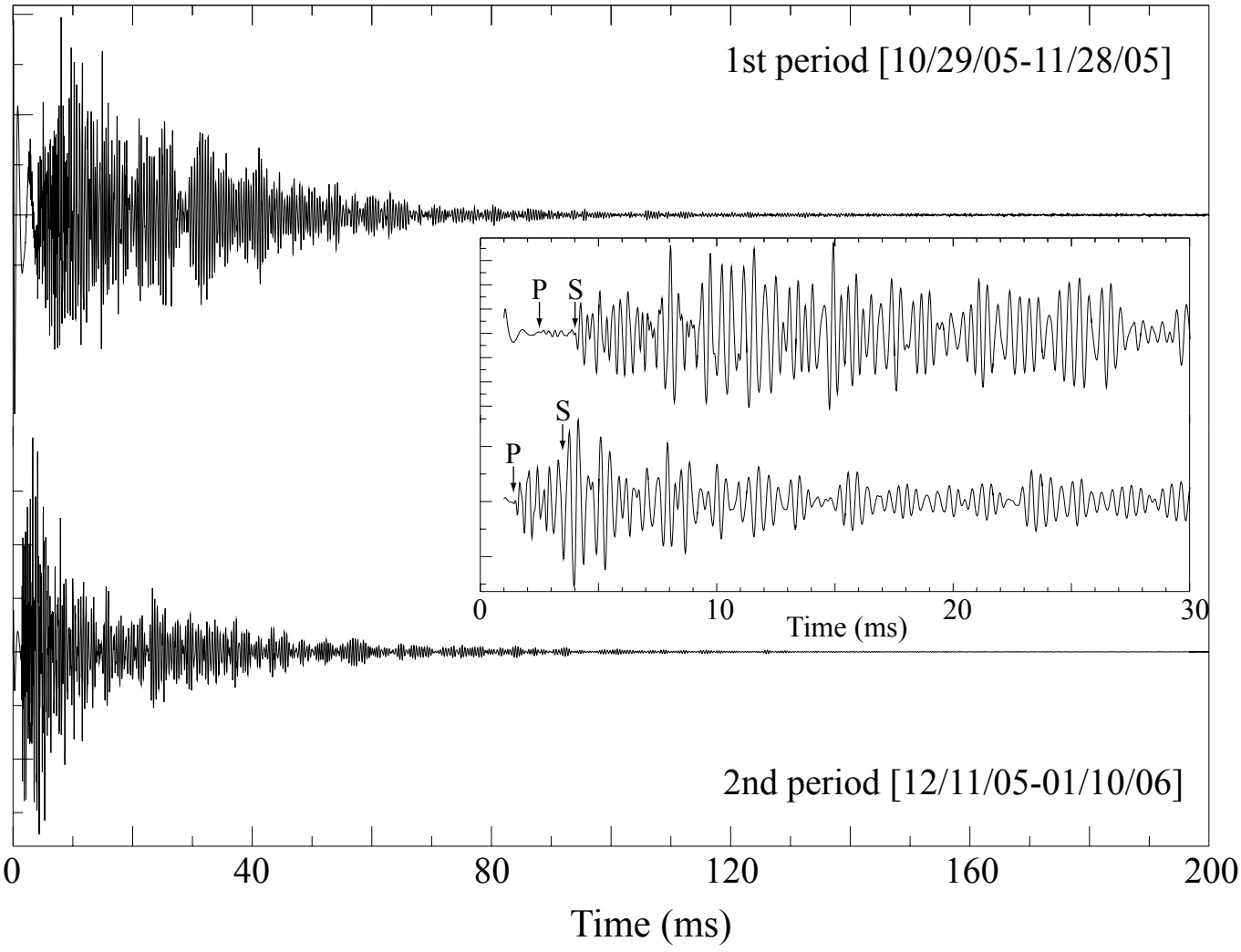
1st period [10/29/05-11/28/05]
P
S
S
P
0
10
20
30
Time (ms)
2nd period [12/11/05-01/10/06]
0
40
80
120
160
200
Time (ms)

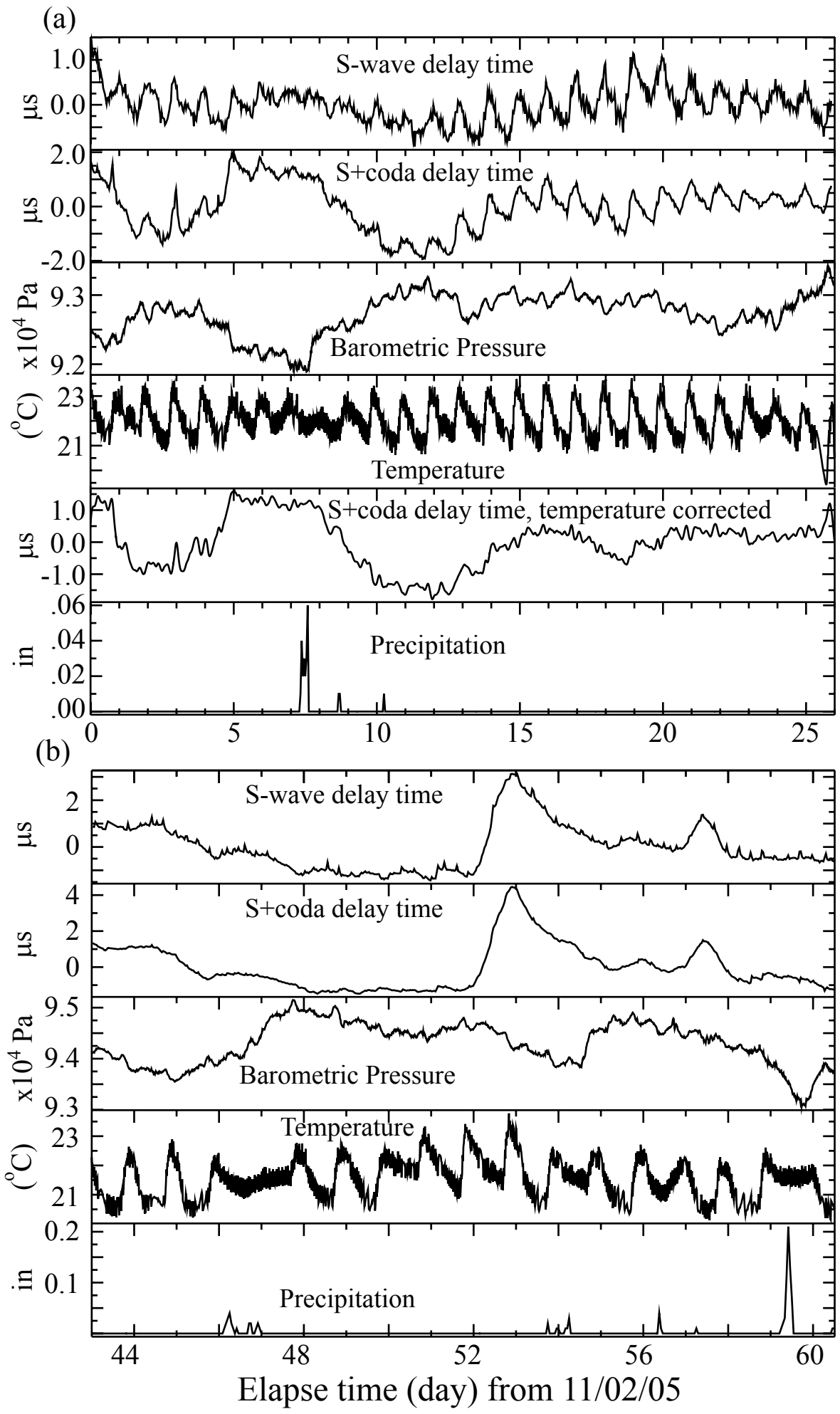
(a)
S-wave delay time
μs
1.0
0.0
S+coda delay time
2.0
0.0
-2.0
Barometric Pressure
x10^4 Pa
9.3
9.2
Temperature
(°C)
23
21
S+coda delay time, temperature corrected
1.0
0.0
-1.0
Precipitation
in
.06
.04
.02
.00
0
5
10
15
20
25
(b)
S-wave delay time
2
0
S+coda delay time
4
2
0
Barometric Pressure
9.5
9.4
9.3
Temperature
23
21
Precipitation
0.2
0.1
44
48
52
56
60
Elapse time (day) from 11/02/05

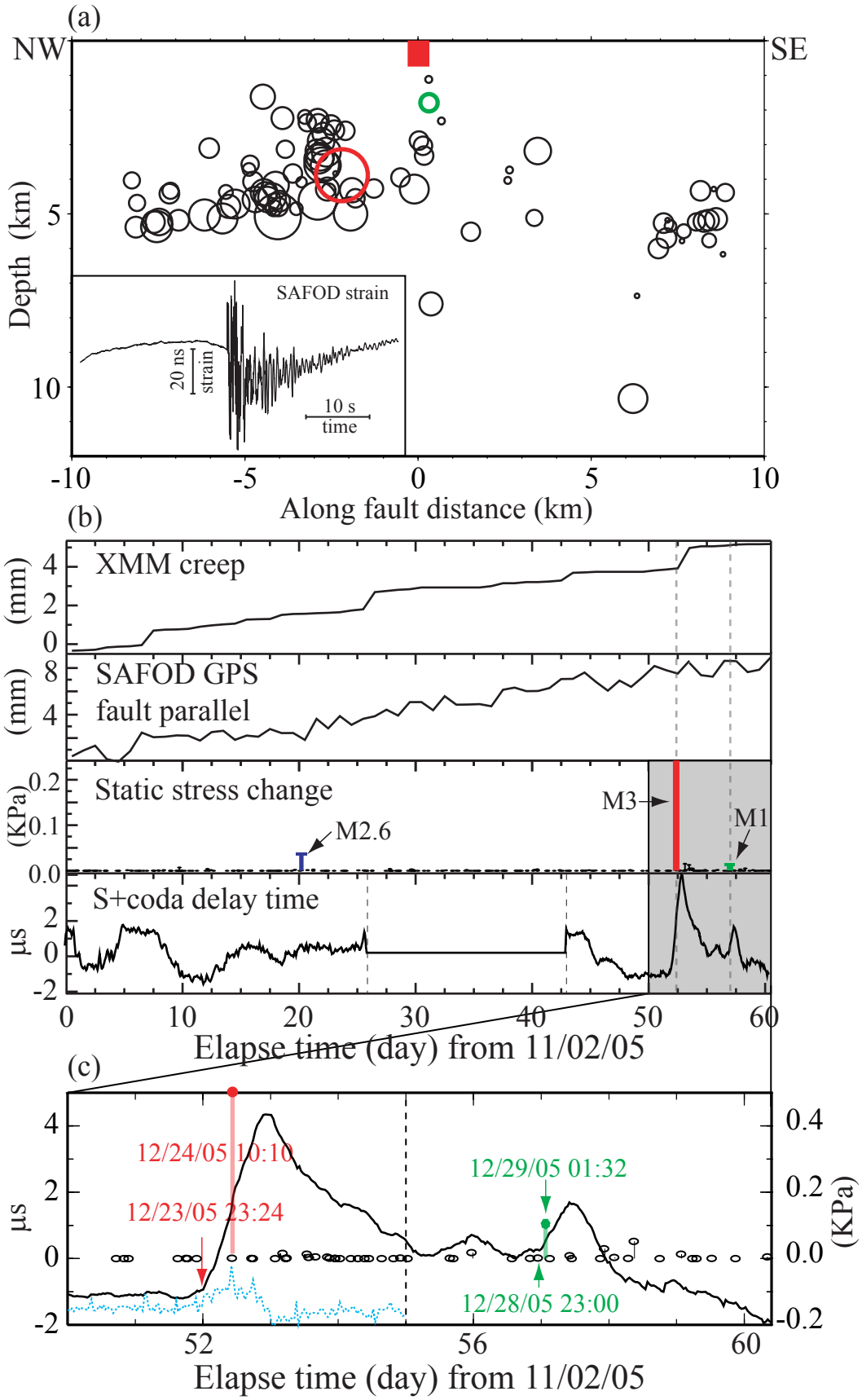
(a)
NW
SE
Depth (km)
5
10
SAFOD strain
20 ns
strain
10 s
time
-10
-5
0
5
10
Along fault distance (km)
(b)
XMM creep
(mm)
4
2
0
SAFOD GPS
fault parallel
(mm)
8
4
Static stress change
(KPa)
0.2
0.1
0.0
M2.6
M3
M1
S+coda delay time
μs
2
0
-2
0
10
20
30
40
50
60
Elapse time (day) from 11/02/05
(c)
μs
4
2
0
-2
12/24/05 10:10
12/23/05 23:24
12/29/05 01:32
12/28/05 23:00
0.4
0.2
0.0
-0.2
(KPa)
52
56
60
Elapse time (day) from 11/02/05